PAPER

Molecular dynamics simulation of adsorption and separation of xylene isomers by Cu-HKUST-1†

Guo-Jian Ji, [ID] *[ab] Ting Xiang,[a] Xiao-Qing Zhou,[a] Le Chen,[b] Zhi-Hui Zhang, [ID] [b] Bei-Bei Lu[a] and Xing-Jian Zhou [ID] [a]

Metal–organic frameworks (MOFs) are widely used in the adsorption separation of various gases. A fundamental understanding of the effective separation of xylene isomers helps improve aromatic products' separation efficiency and reduce industrial separation costs. Grand Canonical Monte Carlo (GCMC) simulations combined with Molecular Science is widely used to predict gas adsorption and diffusion in single crystals with metal–organic frameworks. We performed a GCMC + MD combined approach to study xylene isomers' adsorption and separation in Cu-HKUST-1 to predict the permeability and selectivity of the ternary gas mixture in the MOF with the adsorption and diffusion usage data. Most current studies take into account the computational cost and difficulty. Most recent research models are limited to the adsorption of a single or specific molecule, such as hydrogen, methane, carbon dioxide, *etc.* For this reason, we report an attempt to study the adsorption separation of aromatic gases (*p*-xylene/*o*-xylene/*m*-xylene) based on Cu-HKUST-1 single-crystal materials based on some previous research methods with an appropriate increase in computational cost. To predict the adsorption selectivity and permeability of the ternary mixture of xylene isomers on the MOF surface, the model simulation calculates key parameters of gas adsorption, including gas adsorption volume (N), the heat of adsorption (Q_{st}), Henry coefficient (K), and diffusion coefficient (D).

1 Introduction

Xylene isomers (Fig. 1), are important raw materials for the manufacture of various high value-added chemicals and polymers, respectively.[1] *para*-Xylene (*p*-xylene, PX) is a critical material for the preparation of polyethylene terephthalate
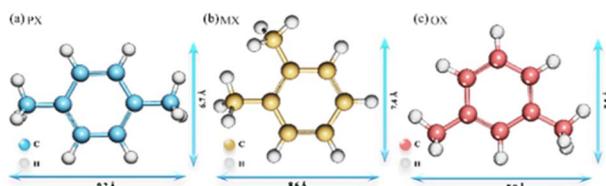

Fig. 1 Structure and molecular size of xylene isomers.

aJiangsu Key Laboratory of Green Process Equipment, School of Petroleum and Gas Engineering, School of Energy, Changzhou University, Changzhou, 213164, P. R. China. E-mail: jgj@cczu.edu.cn; Tel: +86-15806128724

bJiangsu Key Laboratory of Advanced Catalytic Materials and Technology, Advanced Catalysis and Green Manufacturing Collaborative Innovation Center, Changzhou University, Changzhou 213164, P. R. China

† Electronic supplementary information (ESI) available: Detailed inputs for LAMMPS (ZIP), force field details, grand canonical Monte Carlo simulation details, density functional theory simulation details characterization details, and other support charts and tables. See DOI: https://doi.org/10.1039/d2ra06873g

(PET), polyesters, and synthetic resins. *ortho*-Xylene (*o*-xylene, OX) is a common raw material for phthalic anhydride and plasticizers. *meta*-Xylene (*m*-xylene, MX) is mainly used for the synthesis of iso-phthalic acid, which is further used for the mixing of PET resins. After catalytic reforming of crude oil, these three isomers exist as a mixture. Therefore, the separation of single component gas products from mixed xylene isomers is significant for the petrochemical industry.[2] In terms of current industry development, the separation and purification of chemical products are critical and high consumption processes in the chemical industry.[3] Moreover, the similar physical and chemical properties of the three isomers make them more difficult to be separated. The specific structural parameters of the xylene isomers are shown in Table S1.† Therefore, there is an urgent need to find a less costly separation method and screening of adsorbent materials with high adsorption performance for the separation of xylene isomers. Metal–organic frameworks (MOFs) materials are widely used in the adsorption and separation of chemical products because of their high specific surface area and high porosity, as they have the advantages of high adsorption capacity, high selectivity, and recyclability.[4] In addition, MOFs are promising for hydrogen storage,[5] catalysts,[6] magnetic materials,[7] optical materials,[8] drug release,[9] electrical materials,[10] and other related applications, so they are valuable for research on environmental and energy supply issues.

In this paper, we focus on the adsorption separation of ternary mixed xylene isomers by Cu-HKUST-1, a recent class of promising porous materials for adsorption of gas storage.[11] The structure of Cu-HKUST-1 is shown in Fig. 2(a) and (b) by VESTA version.3.5.7.[12] TEM images were taken on a JEOL JEM2 100 transmission electron microscope at an accelerating voltage of 200 kV. Field-emission SEM images of the samples were taken with a Zeiss Supra 55 microscope at 30 kV are shown in Fig. 2(c) and (d). Cu-HKUST-1 was first proposed by Chui et al.[13] in 1999. The high adsorption capacity and stability of Cu-HKUST-1 are due to the mutual static electricity between the porous structures.[14] The material is described as dimeric coordination of copper coordinated with four carboxylate ligands, and the resulting structure shows a three-dimensional porosity consisting of three types of pore channels. The most interesting feature of this structure is the presence of unsaturated metal centers (copper atoms), whose unsaturated sites become potential strong adsorption sites.[15,16] At the same time, mass transfer limitations need to be understood to use this material effectively. Because adsorbents must rapidly adsorb and diffuse into the interior of Cu-HKUST-1, where they are temporarily trapped (by physical adsorption) and can react at active sites within Cu-HKUST-1 (by chemisorption at open metal sites). Therefore, it is crucial to understand the adsorption mechanism of the adsorbent on the Cu-HKUST-1 surface. However, there are few detailed studies on the mechanism of the effect of MOFs on xylene adsorption, especially at the microscopic level.

On the one hand, David Peralta and Karin Barthelet et al.[15] investigated the xylene adsorption in CPO-27-Ni and zeolite NaY. In Cu-HKUST-1, the metal center is more accessible than that of CPO-27-Ni due to electrostatic interactions playing a greater role. The pore geometry of Cu-HKUST-1 is inherently *para*-selective, but the *para*-selectivity is overcompensated by

electrostatic effects, which overall leads to a slight preference for OX adsorption. However, they contend that for this *para*-site selectivity to prevail, the MOF must have a low electrostatic field to prevent preferential adsorption of other isomers. Bárcia et al.[17] mentioned UiO-66 as the more favorable adsorption of OX compared to other xylene isomers. They concluded that the reverse shape selectivity in the adsorption of xylene isomers could be attributed to the rotational degrees of the molecules' freedom in the small cavities. On the other hand, Tyler G. Grissom et al.[18] used isothermal diffusion experiments to reveal that the diffusivity of xylene in UiO-66 ranged between 10^{-8} and 10^{-12} cm^2 s^{-1}, where the relative diffusivity followed the following trend: OX < MX < PX. Qiao et al.[19] simulated the conformation and heat of adsorption of C8 aromatics (ethylbenzene, *p*-xylene, *o*-xylene, and *m*-xylene) in MIL-125 by Materials Studio software. The results showed that among these four isomers, the heat of adsorption of PX and the binding energy of PX in the MIL-125 tetrahedral cage was the largest, so the adsorption of PX was characterized to be greater than the other isomers. The reason is that PX and EB can be adsorbed in both the tetrahedral and octahedral cages of MIL-125, MX and OX can only be adsorbed in the octahedral cages, and the binding energy of the four isomers in the tetrahedral cage is higher than that in the octahedral cage. PX has the highest binding energy in the tetrahedral cage, which may be the reason for the preferential adsorption of PX in MIL-125. Therefore, the adsorption of xylene in MOFs is still controversial.

So far, most reported computational models are limited to a simple small molecule or other specific molecules, such as hydrogen, methane, nitrogen, carbon dioxide, the mixture of CO$_2$/H$_2$,[20] the mixture of CH$_4$/H$_2$ etc.[21] Grand Canonical Monte Carlo (GCMC) method is widely used with Equilibrium Molecular Dynamics (EMD) to predict gas adsorption and diffusion in the single crystals of MOFs. Several studies[1,2,16,21,22] have evidenced the great potential for using GCMC + MD numerical simulation to screen the adsorption properties of a large number of materials. We combine adsorption and diffusion data from these simulations to predict the gas permeability and selectivity of MOF membranes.[21,22] Z. W. Qiao et al.[2] studied the separation of xylenes in MOF by adsorption in concert with the high throughput screening (HTS) method and machine learning (ML) method. The results showed that pore limit diameter (PLD) and larger cavity diameter (LCD) have greater importance. While this study provides useful insight into the separation of xylenes in MOFs, several points need to be noted. First, the initial screening was based on a rigid MOF without consideration of framework flexibility. In principle, this is acceptable because there is no universal transferable force field to accurately describe the flexibility of the various MOFs. The flexibility of the framework as demonstrated according to the article may also strongly affect the separation performance, especially the selectivity. Sütay et al.[23] used Monte Carlo (MC) and Molecular Dynamics (MD) simulations to study the adsorption of dihalogen molecules on raw graphene surfaces, focusing on adsorption sites, adsorption capacities, coverage factors, adsorption isotherms, and adsorption kinetics. The adsorption energies of all adsorbates were also calculated. It is
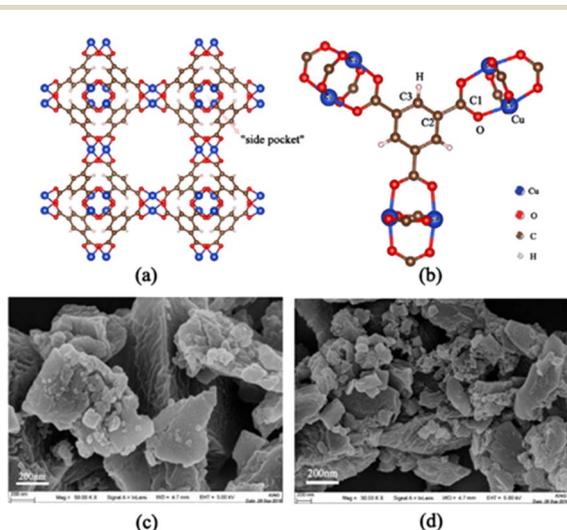

Fig. 2 (a) Two-dimensional structure of Cu-HKUST-1, where the smallest pore, usually named "side pocket", has a pore diameter of 4.6 Å, inaccessible to any xylene isomer. Eight side pockets are arranged in the four corners of a cube, forming two types of large pores with internal diameters of 10 Å and 12 Å. (b) The potential functions of the atoms are named. (c) and (d) SEM structure diagram.

also mentioned that MD simulations can reproduce the real adsorbent effects compared to experimental chemisorption and physical adsorption data in the literature. In addition, DFT is one of the most effective methods to study the adsorption properties of gases. Grissom *et al.*[18] used DFT to calculate the interaction of toluene with the UiO-66 tetrahedral cavity, Perdew–Burke–Ernzerhof general functions for periodic DFT calculations of the cell, and VASP for projection-enhanced wave potential and empirical dispersion correction.

In this study, we focus on the adsorption properties of xylene isomers on the surface of the composite Cu-HKUST-1 using the numerical simulation method GCMC + MD in EMD. The results (N, Q_{st}, K, D) of GCMC simulations (amount of gas load adsorbed) are used as inputs for MD simulations to calculate evaluation parameters, such as adsorption selectivity (S_{ads}), diffusivity (S_{diff}), and permeability (P). These evaluation parameters provide helpful guidance for better studying the adsorption characteristics of the Cu-HKUST-1 film.

2 Computational methods

2.1 Potential energy model

The four atom types for the xylene isomer molecule: C_A, C_T, H_A, and H_T, see Fig. S1.† The atomic foot labeled A belongs to the carbon atom on the aromatic ring, and the trace labeled T belongs to the part forming the methyl group. C_{A1} and C_{A2} are the aromatic C atoms with H and CH_3, respectively. Interaction between PX, MX, and OX molecular mixtures and pore walls of metal–organic architecture materials using the amber force field developed by W. D. Cornell *et al.*[24] For the total potential parameter values used for the simulation process, see Tables S2 and S3.† The total potential energy of the adsorption complex can be divided into four parts of energy composition, see eqn (1).

$$V_{total} = V_{intraxylene} + V_{intra\_mof} + V_{xylene–xylene} + V_{xylene\_mof} \quad (1)$$

$V_{intraxylene}$ is the intramolecular potential energy of the xylene molecule, V_{intra_mof} is the potential energy within the Cu-HKUST-1 crystal structure, and $V_{xylene–xylene}$ is the potential energy between the molecules of the xylene isomers, V_{xylene_mof} is the internal potential energy of the xylene isomer molecule with the Cu-HKUST-1 crystal structure.

The functional form of the total potential includes: harmonic potential with bond length ($V_{stretch}$) and angle (V_{bend}) as units. The equilibrium bond lengths and bond angles were obtained by charge derivation using the split valence 6-31g(d,p) basis sets at the Hartree–Fock (HF) approximation level. ($V_{torsion}$) is energy involved in dihedral angles. The values of point charges are estimated from the wave functions of isolated molecules according to the extended charge equilibration (EQ_{eq})[25] scheme, and the point charges of atoms of the same type are equalized to their average values.[26] The first three summations are for the appropriate coordinates, and the last summation is for all "non-bonded" intramolecular distances, see eqn (2).

$$V_{xylene} = V_{stretch} + V_{bend} + V_{torsion} + V_{vdw} + V_{coul}$$

$$= \sum \left(\frac{k_r}{2}(r - r_0)^2 \right) + \sum \left(\frac{k_\theta}{2}(\theta - \theta_0)^2 \right)$$

$$+ \sum k[1 + \cos(n\phi - \delta)] + \sum \left(4\varepsilon_{ij} \left[\left(\frac{\sigma_{ij}}{r_{ij}} \right)^{12} - \left(\frac{\sigma_{ij}}{r_{ij}} \right)^6 \right] + c \frac{q_i q_j}{r_{ij}} \right)$$

$$(2)$$

In the simulations, the non-bonding interaction potentials between the molecules of PX, MX, and OX gases and the bonding potential energy between the internal molecules are described by the Lennard–Jones (LJ) 12–6 possible energy model for both intermolecular van der Waals interactions (V_{vdw}) and electrostatic interactions treated by Coulomb interactions (V_{coul}). The pair of particles i and j with relative distance r_{ij}, their interaction potential energy is shown in eqn (3).

$$\phi(r_{ij}) = 4\varepsilon_{ij} \left[\left(\frac{\sigma_{ij}}{r_{ij}} \right)^{12} - \left(\frac{\sigma_{ij}}{r_{ij}} \right)^6 \right] \quad (3)$$

where σ and ε are the LJ molecular diameter and potential energy. i and j can refer to PX, MX, and OX molecules, respectively. The parameters of the solid (Cu-HKUST-1)-fluid (PX, MX, and OX) interactions were calculated using the Lorentz–Berthelot combination rule obtained, see eqn (4).

$$\sigma_{ij} = \frac{\sigma_i + \sigma_j}{2} \text{ and } \varepsilon_{ij} = (\varepsilon_i \varepsilon_j)^{\frac{1}{2}} \quad (4)$$

Finally, the simulations were performed at infinite dilutions, and we neglected the intermolecular interactions between adsorbents and adsorbents. The charge of Cu-HKUST-1 is allocated using an approximate charge allocation method. Computational cost is critical in large-scale molecular structure studies, and many assumptions are made to reduce the computational power and time required. In this study, we defined the skeleton of Cu-HKUST-1 as a rigid structure and applied the universal force field (UFF) described by A. K. Rappe *et al.*[27] and the DFF force field to the skeleton structure in the simulation process. Detailed parameters are shown in Fig. S2 and Table S4.† When using the force field, we preferentially choose the DFF force field, considering that the DFF force field has no transition element Cu, and then use the UFF force field.

2.2 Simulation detail

2.2.1 GCMC calculation. The GCMC method is described in ESI S3.† We used RASPA[28] to simulate the adsorption properties of the xylene isomer gas mixture by the GCMC method. In the simulation process, the simulation unit composed of Cu-HKUST-1 crystal structure with xylene isomer molecules was defined, and periodic boundary conditions were applied in the x, y, and z axes. Simulation early in keeping the system volume, under the premise of constant temperature and adsorption potential energy, the particles in the random selection system translational action. The system's power tends to decrease with a certain probability after receiving it. Pressure, temperature,

and mixture were selected as control variables to simulate the adsorption behavior of mixed gas under different parameter combinations. The temperatures were selected including 348 K, 373 K, and 398 K. The pressure range was 1–1000 Pa. In the simulation process, the GCMC method is used in RASPA to set the number of loop simulation steps to 100 000 and the balance steps to 20 000. The external temperature control was 298 K, and the thermostat time scale was 0.15 ps. The pressure regulator time scale parameter was 0.15 ps. The cross-term was first tested using the Lorentz–Berthelot mixing rule, and the full host–guest interaction calculation was used for the test. The potential energy was calculated using spherical truncation and the truncation radius of fluid intermolecular interaction was 13 Å.

2.2.2 MD calculation. The molecular dynamics component was calculated using the Large-Scale Atom/Molecular Weight Parallel Simulator (LAMMPS).[29] Based on the $1 \times 1 \times 1$ Cu-HKUST-1 cell unit model (Fig. 3), a $3 \times 3 \times 3$ supercell model structure was established by cell expansion. The size of the supercell model is $a = 79.029$ Å, $b = 79.029$ Å, $c = 79.029$ Å. Using the UFF force field between molecules and the skeleton, AMBER force field for the description of the force field between molecules of adsorbate materials. Periodic boundary conditions were applied with cutoff of 13 Å, and a time step of 1 fs was used for all simulations. Use the Nosé–Hoover thermostat to balance each run by 100 ps in the canonical NVT (constant atomic number, volume, and temperature) ensemble.

After model initialization, energy minimization, and atomic interaction configuration, the gas adsorption of xylene isomers in rigid Cu-HKUST-1 was investigated at three temperatures (348 K, 373 K, and 398 K) respectively. We mainly use molecular dynamics to calculate the diffusivity of each xylene isomer gas particle in limited system size, and the Mean Square Displacement obtains the diffusivity (MSD),[30] as indicated in eqn (5). MSD is the average ensemble after balance, and the sequential n-order algorithm[31] used to measure MSD can capture the correlation, in short, medium, and long-time conveniently and effectively.[32,33] The MSD for all molecular dynamics runs was calculated every 100 timesteps using the centroid form. It is worth noting that the effect of any drift in the mass of atoms in this study was subtracted before calculating the displacement of

each atom.[34] The data are processed as 250 uniformly distributed multiple time starting points, and the diffusivity (D) is estimated from the slope of MSD over the time interval δ_t by the Einstein relation (eqn (6)),[35] with d_α being the spatial dimension ($d_\alpha = 3$).

$$\text{MSD}(t) = \frac{1}{N_\alpha} \left(\sum_{i=1}^{N_\alpha} [r_i^\alpha(t_0 + t) - r_i^\alpha(t_0)]^2 \right) \tag{5}$$

where N_α is the number of molecules or atoms in component α, t is time, and $(t_0 + t) - (t_0)$ is the vector distance traveled by particle i in component α in a period.

$$D = \frac{1}{2d_\alpha} \lim_{t \to \infty} \frac{d}{dt} \left(\frac{1}{N_\alpha} \sum_{i=1}^{N_\alpha} [r_i^\alpha(t_0 + t) - r_i^\alpha(t_0)]^2 \right) \tag{6}$$

2.2.3 Charge calculation. E. W. Christopher et al.[36] developed an extended charge balance (EQ$_{eq}$) method that includes all available ionization energies for each atom in the periodic table to estimate the charge of Cu-HKUST-1. As for the charge part, two charge calculation schemes, EQ$_{eq}$ and DFT, were carried out. Although DFT computes charges more accurately, EQ$_{eq}$ charges perform as well as electrostatic potentials due to the more extensive computational system. EQ$_{eq}$ requires only a fraction of the computational cost, and approximation schemes such as the EQ$_{eq}$ method may produce reasonable predictions in less time. We simultaneously compare the changing trend of the two charge calculation results (Fig. 4). DFT calculated the atomic charge of the xylene isomer. Considering the large model of metal–organic frame structure and a large number of atoms, the atomic charge of the frame structure was calculated by EQ$_{eq}$. See charge calculation details in ESI S3.†

3 Results and discussion

3.1 Characterization of Cu-HKUST-1

We used Zeo++ v0.3 version[37] to characterize the structure of Cu-HKUST-1 in terms of pore limit diameter (PLD), maximum cavity diameter (LCD), body surface area (S_{BET}), free volume (V_{free}), and porosity (φ). Table S6† shows the detailed parameters. The spherical probe (N$_2$) measures the pore structure distribution. This analysis gives an exact distribution of the
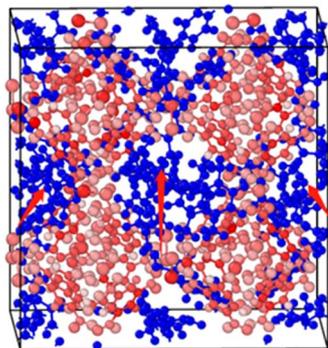

Fig. 3 Adsorption conformation of the xylene isomers on a $1 \times 1 \times 1$ Cu-HKUST-1 cell model. In this figure, the xylenes can only pass through the channels due to the largest size of Cu-HKUST-1.
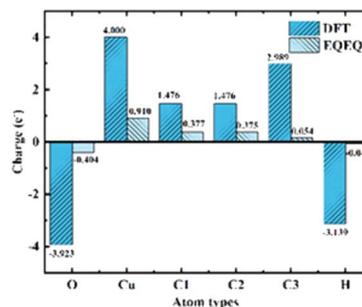

Fig. 4 Comparison of charge calculated by EQ$_{eq}$ and DFT. Atomic types are illustrated in Fig. 2(b).
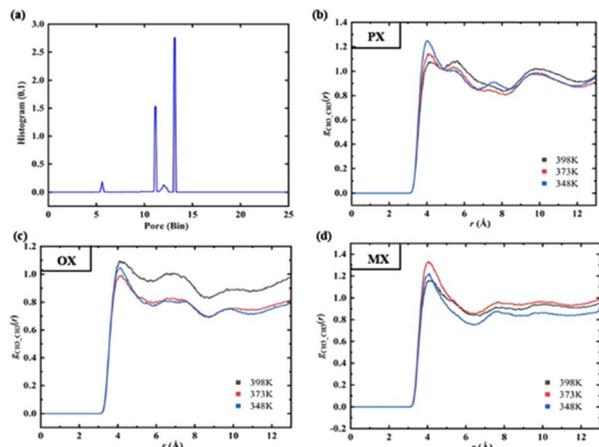
Fig. 5 (a) Histogram of the pore size distribution (PSD). (b–d) RDF between −CH$_3$ group of xylenes at different temperatures.

pore size for materials consisting of spherical, cylindrical, or slit-type pores. This geometric pore size definition is still fully applicable to irregular materials.[38] The pore size distribution (PSD) Fig. 5(a) is calculated geometrically in Zeo++ by using the Voronoi methods (Fig. S6†).

The PSD gives information about the size of specific pores corresponding to each point in the void volume, finding the giant sphere that encloses the issue but does not overlap with any frame atom, which gives the cumulative pore volume curve.[39] For the principle of the analysis, see Fig. 5(b–d). In the present study, each cell is set up with 5000 Monte Carlo

samples, and the fraction of sample points in the nodal sphere is 0.38, where the minimum atomic radius is 1.2 Å, while the maximum atomic radius is 1.7 Å. By default, the histogram has 1000 containers of size 0.1 Å. It is recommended to use a detection radius similar to the atomic radius, which should have a peak accuracy of 0.1 Å. Some material characterization supplements for Cu-HKUST-1 are included in ESI S5.†

3.2 Adsorption of xylene isomers

3.2.1 Gas uptake. The basic concepts of adsorption science are adsorption isotherms, which describe the interaction between adsorption and adsorbent.[40] In this paper, the adsorption isotherms of xylene isomers in Cu-HKUST-1 were described using the GIBBS ensemble method.[41] Fig. 6 shows the adsorption isotherms of Cu-HKUST-1 for single components (a), (b), (c) and ternary mixed components (d), (e), (f) at 348 K, 373 K, and 398 K, respectively. The selectivity trend for ternary mixtures is the same as that for single components. In Fig. S7,† this selectivity with increasing pressure is consistent with the previous breakthrough experiments at 398 K.[43] The characterized adsorption order (OX > PX > MX) obtained by simulation is consistent with the experiment at the highest temperature of 398 K. However, the gas uptakes obtained by simulation is significantly higher than the experimental data, which may be related to the influence of impurity error in the experimental process. Moreover, the rigid metal–organic frameworks used in the simulation have better adsorption and separation performance. In the adsorption process of single components and ternary mixed components, the increasing temperature leads to a decrease in the total adsorption capacity of the channel. The
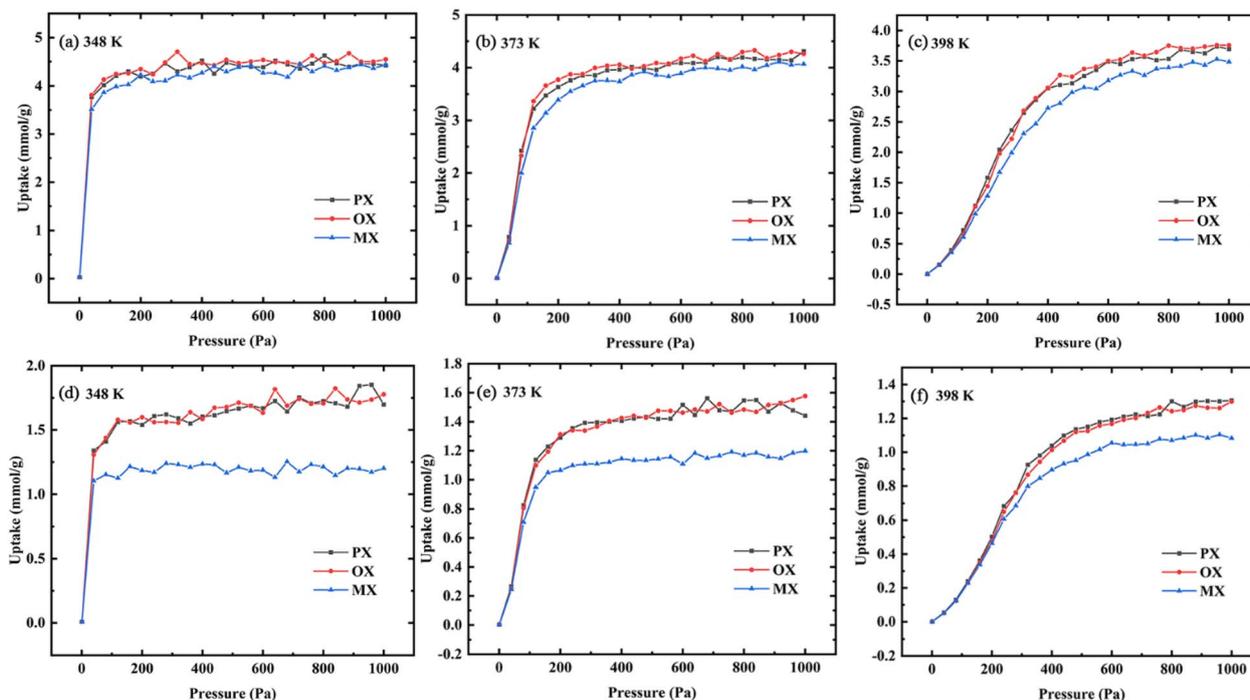

Fig. 6 Adsorption isotherms of single-component (a–c) and ternary mixed component (d–f) in Cu-HKUST-1 at different temperatures (PX, square; OX, circular; MX, triangle).

isotherms at 348 K and 373 K are much steeper than the isotherms at 398 K. This may be due to the effect of temperature on the structure of the metal–organic skeleton, resulting in the change of the frame structure with temperature. In the equimolar ternary mixture, Cu-HKUST-1 showed significant selectivity for MX/OX and MX/PX with the change of temperature. The adsorption tendency of OX and PX was better than MX, but the adsorption capacity of each isomer component in the single component was not much different.

Adsorption selectivity (S_{ads}) is a crucial research index to evaluate the separation performance of MOF adsorbed gas.[42,44] The ideal selectivity is calculated as the ratio of the single component absorption (N) of the more adsorbed gas component (i) to the absorption of the other gas species (j) at a predetermined pressure (eqn (7)). The separation simulation results of equimolar mixed xylene isomeric components on Cu-HKUST-1 material are shown in Table 1. Selectivity values (S_{ads}) for separation of binary mixtures of xylenes as shown in Fig. 7.

$$S_{ads} = N_i/N_j \qquad (7)$$

Compared with several MOFs with better separation performance of xylene isomers, it is found that most MOF materials are better selective for OX than the other two isomers (Table 1). MOF-5 exhibit PX preferential adsorption in low pressure. As pressure increases, MOF-monoclinic adsorption to PX increases significantly, and OX and MX adsorption do not change

significantly.[45] CPO-27-Ni and Cu-HKUST-1 have similar separation behaviors, both are OX selective adsorbents, MX and PX are saturated before OX. However, the separation selectivity of CPO-27-Ni is higher than Cu-HKUST-1. Cu-HKUST-1 is inherently less selective for PX, with little apparent separation observed for MX/PX mixtures. The layered Cu-HKUST-1 microcrystals obtained in this work show better separation ability for PX than previously reported Cu-HKUST-1 single crystals under similar conditions, while other MOFs as a whole show no obvious selection advantage for PX.[43,46] At low pressure, OPLS and charged AUA models predicted that UiO-66 was selective to OX over the entire pressure range. Trappe expanded models predict higher *para*-xylene capacities at pressures higher than 3–7 kPa. The results show that the adsorption capacity of OX is higher than that of other isomers, and the least adsorption is PX.[47] CD-MOF-1 has high selectivity for xylene isomers. The maximum separation for OX/PX is shown at 298 K and 318 K in CD-MOF-1, and the dynamic adsorption capacity for PX increases with temperature increase. At 318 K, PX and MX first elute as a mixture, which is similar to MIL-53 (Al).[48,54] In terms of separation factor Co_2 (dobdc) and $Co_2(m$-dobdc) performed better than NaY separation of industry-related zeolite materials.[49] Both the experiment and the molecular simulation show that MIL-47 has great adsorption selectivity to xylene isomer, the selectivity factor obtained at low temperatures is larger than that of the experiment. The MIL-53 of xylene (Al) is the strongest in OX adsorption. Compared with MIL-53 (Al), MIL-47 has a smaller aperture (about 6 Å) and exhibits better xylene

Table 1 Overview of separation selectivity for xylene isomers on MOFs

Adsorbent	T (K)	Adsorption capacity (mmol g^{-1})			Separation selectivity (S_{ads})			Adsorption trend	Ref.
		PX	OX	MX	OX/MX	MX/PX	OX/PX		
MOF-5	423	—	—	—	0.53	1.21	0.65	MX > PX > OX	45
	553	—	—	—	1.07	1.78	1.91	OX > MX > PX	45
MOF-monoclinic	423	—	—	—	2.24	0.23	0.52	OX > MX > PX	45
	453	—	—	—	0.58	0.24	0.14	PX > MX > OX	45
CPO-27-Ni	398	—	—	—	1.67	2.00	3.33	OX > MX > PX	43
	298^a	—	—	—	0.4	0.8	0.7	PX > MX > OX	46
Cu-HKUST-1	348	1.70	1.78	1.20	1.47	0.71	1.05	OX > PX > MX	This work
	373	1.44	1.58	1.20	1.31	0.83	1.09		This work
	398	1.31	1.30	1.08	1.20	0.82	1.00		This work
NaY	398	—	—	—	0.63	2.50	1.43	MX > OX > PX	43
UIO-66	398	—	—	—	6.87	1.36	9.35	OX > MX > PX	47
	423	0.14	1.24	0.21	7.30	1.23	8.95		47
CD-MOF-1	298	—	—	—	5.7	1.9	10.8		48
	318	—	—	—	6.1	1.3	7.9		48
Co$_2$(dobdc)	306^a	—	—	—	2.5	1.6	3.9		49
	298^a	—	—	—	—	0.4	^{b}		50
	343^a	—	—	—	1.17	2.07	1.01		51 and 52
MIL-47	343	—	—	—	8.2	5.7	1.4		52
	383	—	—	—	3.5	3.0	1.5		51
	423	—	—	—	3.2	1.9	1.5		51
	298	—	3.37	—	2.7	^{b}	3.5		53
MIL-53 (Al)	313	—	6.76	—	2.1	—	2.1		54
	323	—	—	—	1.58	1.83	2.53		54

^{a} Experimental values obtained from breakthrough experiments. ^{b} Two isomers could not be separated.
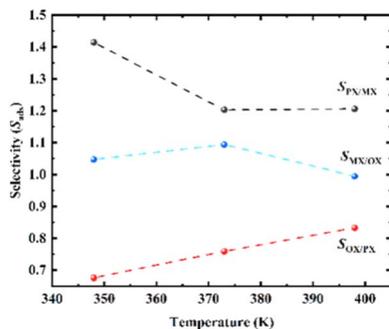
Fig. 7 Selectivity values (S_{ads}) for separation of binary mixtures of xylenes on Cu–HKUST-1 at 1000 Pa.

selectivity. Cu–HKUST-1 OX is retained preferentially over the other two isomers, similar to the performance of MIL-53 (Al). Compared to MIL-53 (Al), MIL-47 has a preference for PX and shows poor selectivity between OX.[50]

The Langmuir and Freundlich models were used to fit the absolute adsorption curves nonlinearly, some properties of the adsorbent were derived from the model fitting parameters (Table S7†).[55] The isotherm constants and correlation coefficients were fitted as shown in Table S8.† The Langmuir and Freundlich isotherm models were statistically significant at the 95% confidence level. We discussed the shape of the isotherms to predict the desirability of the adsorption system. We found that the adsorption of Cu–HKUST-1 on xylene isomers correlated well with the adsorption of the Langmuir equation ($r^2 > 0.95$), whereas the adsorption of Cu–HKUST-1 on xylene isomers correlated poorly with the adsorption of the Freundlich equation ($r^2 < 0.95$). Therefore, according to the requirement of correlation coefficient $r^2 > 0.95$, the isotherm of adsorption of Cu–HKUST-1 on xylene isomers coincides with the conditions for fitting the Langmuir equation.

3.2.2 Adsorption heat. The heat generated by the adsorption process is the adsorption heat, which can accurately represent the adsorption phenomenon's physical or chemical nature, the activity of the adsorbent, and the strength of the adsorption capacity.[35] The magnitude of the adsorption heat shows the ability of adsorption. The greater the adsorption heat, the stronger the adsorption capacity. The heat of adsorption obtained under different pressure conditions can be statistically analyzed. Using the fluctuation method under the ideal gas hypothesis, the isothermal adsorption heat can be easily calculated from GCMC simulation. Isothermal adsorption heat can be calculated by eqn (8).

$$Q_{st} = H_b - \left[\frac{\partial(U_a)}{\partial N}\right]_{T,V} \quad (8)$$

where H_b is the enthalpy of the bulk phase, U_a is the energy of the adsorption phase, and N is the number of adsorbed molecules. The adsorption heat of xylene isomers in Cu–HKUST-1 is shown in Table 2. The heat comparison of adsorption under equimolar mixing at different temperatures is shown in Fig. 8.

Table 2 Adsorption heat of xylene isomer in Cu–HKUST-1 at 1000 Pa (kJ mol^{-1})

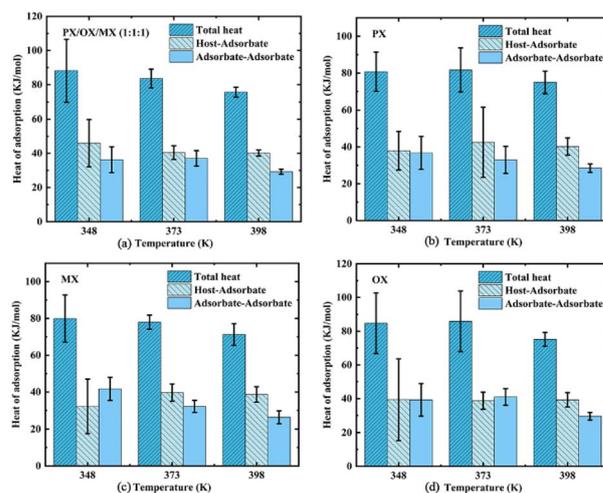| T (K)	Total heat	Host–adsorbate	Adsorbate–adsorbate
PX/OX/MX (1 : 1 : 1) _1000 Pa			
348	88.200	45.933	36.222
373	83.589	40.401	37.018
398	75.705	40.179	29.260
PX_1000 Pa			
348	80.717	37.977	36.767
373	81.706	42.521	32.988
398	74.968	40.222	28.473
OX_1000 Pa			
348	84.711	39.432	39.273
373	85.870	38.707	40.984
398	75.170	39.262	29.619
MX_1000 Pa			
348	79.948	32.292	41.681
373	77.979	39.653	32.197
398	71.230	38.669	26.351

Fig. 8 The comparison of adsorption heat and overall adsorption heat between adsorbent and adsorbent at different temperatures and the correlation error analysis.

Combinations of potential energy functions for all positions and directions of the gas molecules were used to generate configurations. These integrals are solved in GCMC simulations to obtain the probability densities of gas molecules at different adsorption sites. Such densities reflect minor differences in the adsorption heat. Further insight into the interaction energy trend of the xylene isomer with the adsorbent surface can be obtained by observing the simulated probability densities at the PX, MX, and OX positions, respectively, in the Cu–HKUST-1 material (Fig. 9). It reflects the slight difference in adsorption heat. As a result of the interaction between the adsorbent and Cu–HKUST-1, the adsorption molecular dynamics size is large, preventing the entry of molecules through micropores and mesopores.
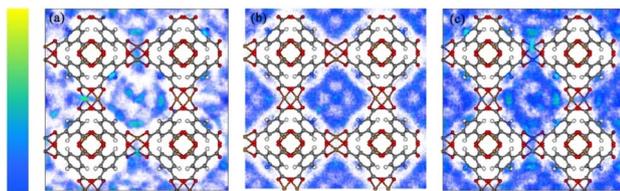
Fig. 9 Probability density plot of adsorbate locations in Cu–HKUST-1 generated by Monte Carlo NVT simulations. (a) PX, (b) MX, and (c) OX. The yellow region is stronger than the blue region. Adsorption density of PX at 348 K and 398 K (Fig. S8†).
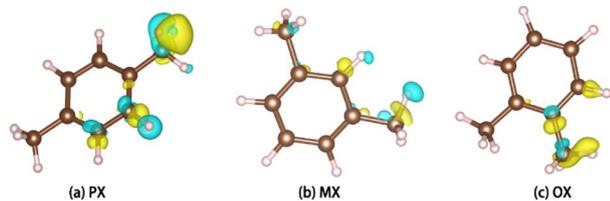

Fig. 10 Charge difference diagram.

PX, MX, and OX isomers lose electrons at the hydrogen end after adsorption, and the charge distribution of hybrid orbitals around the carbon atom changes. Charge difference means that the three isomers interact strongly with the metal skeleton (Fig. 10).

3.2.3 Henry's constants. In order to evaluate the gas-adsorbent interaction and predict the capture and separation performances of xylene isomers under dilute conditions for Cu-HKUST-1. We calculated Henry's constants (eqn (9)) based on single component sorption isotherms by using RASPA as shown in Table 3, the Henley coefficients of the xylene isomers in Cu-HKUST-1 are the same within a deviation of less than 1%. The Henry coefficient was often used to describe the affinity between the adsorbate molecules and the porous frameworks. Henry's constant is a useful measure of the adsorbent affinity for adsorbates, because it represents the partition of the adsorbate between its bulk phase and adsorbed phase at very low pressures.[57]

$$K = \frac{1}{k_B T \rho} \frac{1}{N} \sum_{i=1}^{N} \exp\left(-\frac{U_i}{k_B T}\right) \qquad (9)$$

Table 3 The calculation results and experimental data of Henry coefficient of Cu–HKUST-1 (10^{-4} mol kg^{-1} Pa^{-1})

	T (K)	Method	PX	MX	OX	Ref.
Cu-HKUST-1	298[a]	Simul.	4.4	4.1	3.9	This work
	423	Simul.	1.9	1.6	1.9	43
CPO-27-Ni	423	Simul.	1.9	4.4	4.7	43
MIL-47	543	Simul.	2.3	1.9	2.7	51
		Exptl.	2.2	2.1	2.9	56

[a] Henry's constants were calculated from pure component adsorption isotherms at 298 K.

where T, ρ, N, k_B, and U_i are the adsorbent temperature, density, number of grid points, Boltzmann constant, and the potential energy of a single grid.

Using Henry coefficients to predict the separation performance.[58] The dilution selectivity represents the separation capacity of the material, usually dividing the calculated individual Henry coefficients by the zero loading, see eqn (10).

$$S_{ads} = K_i/K_j \qquad (10)$$

As shown in Table 3, the order of Henry's coefficients is PX > MX > OX, which agrees well with the relative adsorption of xylene isomers at low temperature.[46] By identifying the Henry coefficients from the pure component, the thermodynamic selectivity of MX/PX, OX/MX, and OX/PX were predicted to be 0.93, 0.95, and 0.87 at dilute conditions at 298 K, respectively. The results of the calculation reaffirmed the previous observation that separation performance in Cu-HKUST-1. $S_{PX/MX}$ > 1 indicates that PX is preferentially adsorbed, and $S_{OX/MX}$ < 1 suggests that MX is preferentially adsorbed. However, the OX/PX selectivity of Cu-HKUST-1 is relatively low because the electrostatic interactions favoring OX are offset by weak *para*-selection. With the increase of temperature, Henry's coefficient of OX is the largest. These results further demonstrated that small pores with the narrow pore size distribution of Cu-HKUST-1 could effectively increase the framework-OX interactions and make it expectedly potential for OX capture and separation under dilute conditions.

3.3 Diffusion coefficients

In high-throughput molecular adsorption dynamics simulations, diffusion coefficients are commonly used to calculate the gas diffusivity of MOF materials.[59] The self-diffusion coefficient of xylenes are determined by using Einstein's relation (MSD method). Diffusivity is in turn related to the MSD of the adsorbed gas molecules. The MSD is measured over time to determine whether the fluid is acting due to diffusion alone. We can use the coordinates of each atom, the velocity, or the center of mass of each molecule. The reason we use the center of mass of the molecule in our study instead of the individual atomic coordinates is that when atomic coordinates are used, the vibrational displacements of individual atoms are tracked over a short period while the center of mass displacement performs better.

In Fig. 11, the MSD is plotted as a function of time for 1000 configurations of xylene isomer gas after the equilibrium cycle obtained from the simulation trajectory. Since the MSD accuracy decreases rapidly with time after the MSD becomes linear, we fit the diffusion coefficients from multiple data points and the fit should be limited to the linear diffusion region of the MSD-ΔT curve. The diffusion coefficients of each component are shown in Table 4.

This constant portion of the graph gives the diffusion coefficient. The ballistic region is also seen in Fig. 11 which is the log–log plot of MSD with time and is represented by the parabolic region of the graph very close to origin. In this case, the molecules at the beginning move swiftly in the holes present in
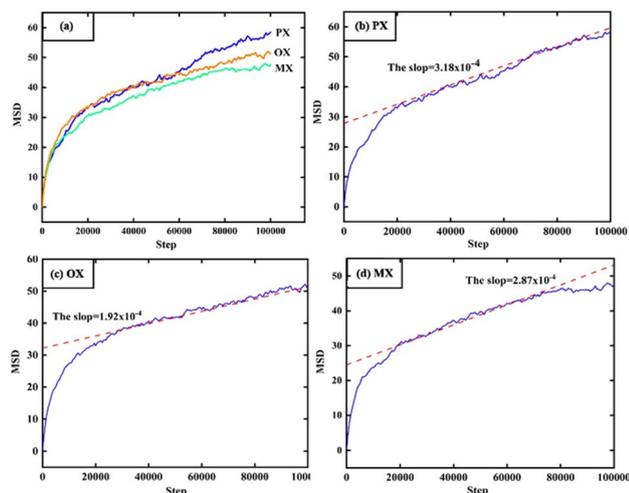
Fig. 11 MSD, results of molecular dynamics (MD) at the 398 K and 1000 Pa.

Table 4 The simulated value of self-diffusion coefficient of PX, OX, and MX at 1000 Pa

	Diffusion coefficient (1×10^{-8} m^2 s^{-1})		
T (K)	PX	OX	MX
348	3.05	2.89	1.98
373	3.20	3.10	2.10
398	3.18	2.87	1.92

the system thereby showing a higher value of diffusion coefficient. After a certain time, the molecules show uniform motion as a result of which we see the linear portion of the plot.

4 Conclusions

In the study, we have found that Cu-HKUST-1 has an unsaturated metal center that contains Cu^{2+}. Therefore, the adsorption site near Cu^{2+} in the cell exhibits more obvious aggregation, mainly due to the interaction between the dipole moment of the xylene molecule and the electrostatic field of the adsorbent. Based on the adsorption uptakes and adsorption heat, the adsorption trend of the mixed gas of xylene isomers between Cu-HKUST-1 was determined: OX $\approx$ PX > MX. The adsorption amount and adsorption heat of each component of mixed xylene isomer showed a decreasing trend with the increase of temperature. The adsorption capacity and adsorption heat at 398 K are inferior to that at 348 K and 373 K. This may be caused by the collapse of the skeleton linker with increasing temperature. By analyzing the adsorption heat, we found that the difference between PX and OX was very small, while the adsorption heat of MX was significantly smaller than that of PX and OX. In contrast to the MX molecule, the small volume of the OX molecule can more readily fill the cavity of the Cu-HKUST-1 molecule. When pores are filled, molecular packing or arrangement effects do not enormously change the adsorption

behavior. Since the interaction between xylene and unsaturated metal centers is much weaker than the interaction between cations outside the skeleton, there is a lower density of adsorbed phase in Cu-HKUST-1. Finally, we assume that Cu-HKUST-1 has a perfect crystal structure. However, in practice, electrostatic interactions between atoms in the crystal may also have an impact on the actual adsorption process, which may lead to an over or underestimation of the material's adsorption capacity.

Author contributions

The manuscript was written with the contributions of all authors. All authors have approved the final version of the manuscript.

Conflicts of interest

There are no conflicts to declare.

Acknowledgements

References

1 J. A. Gee and D. S. Sholl, *J. Phys. Chem. C*, 2015, **120**, 370–376.
2 Z. W. Qiao, Y. L. Yan, Y. X. Tang, H. Liang and J. W. Jiang, *J. Phys. Chem. C*, 2021, **125**, 7839–7848.
3 J. Lannoeye, B. D. Van, V. Belgin, B. Helge and D. D. Vos, *Microporous Mesoporous Mater.*, 2016, **226**, 292–298.
4 X. H. Bu and J. L. Zuo, *Sci. China: Chem.*, 2016, **59**, 927–928.
5 K. K. Gangu, S. Maddila, S. B. Mukkamala and S. B. Jonnalagadda, *J. Energy Chem.*, 2019, **30**, 140–152.
6 J. Hwang, *Korean J. Chem. Eng.*, 2021, **38**, 1104–1116.
7 E. Coronado, *Nat. Rev. Mater.*, 2020, **5**, 87–104.
8 W. Yin, C. A. Tao, F. Wang, J. Huang and J. Wang, *Sci. China: Chem.*, 2018, **61**, 391–400.
9 C. Y. Sun, C. Qin, X. L. Wang and Z. M. Su, *Expert Opin. Drug Delivery*, 2013, **10**, 89–101.
10 D. X. Liu, D. T. Zou, H. L. Zhu and J. Y. Zhang, *Small*, 2018, **14**, 1801454.
11 J. Barreto, M. Xavier, P. Rui, D. Martins and G. Bonfait, *J. Chem. Eng. Data*, 2019, **64**, 5407–5414.
12 K. Momma and F. Izumi, *J. Appl. Crystallogr.*, 2011, **44**, 1272–1276.
13 S. S. Y. Chui, S. M. F. Lo, J. P. H. Charmant, A. G. Orpen and I. D. A. Williams, *Science*, 1999, **283**, 1148.
14 A. Jp, A. Xb, A. Yl, A. By, A. Py, Y. A. Fei and M. Jie, *Environ. Res.*, 2021, **205**, 112425.
15 D. Peralta, K. Barthelet, J. Pérez-Pellitero, C. Chizallet, G. Chaplais, A. Simon-Masseron and G. D. Pirngruber, *J. Phys. Chem. C*, 2012, **116**, 21844–21855.

© 2022 The Author(s). Published by the Royal Society of Chemistry

16 H. Daglar and S. Keskin, *Coord. Chem. Rev.*, 2020, **422**, 213470.

17 P. S. Bárcia, D. Guimares, P. A. P. Mendes, J. A. C. Silva, V. Guillerm, H. Chevreau, C. Serre and A. E. Rodrigues, *Microporous Mesoporous Mater.*, 2011, **139**, 67–73.

18 T. G. Grissom, C. H. Sharp, P. M. Usov, D. Troya, A. J. Morris and J. R. Morris, *J. Phys. Chem. C*, 2018, **122**, 16060–16069.

19 X. Qiao, Y. Liu, Y. Yang, H. Wang, J. Ma, D. Wang, N. Gao, L. I. Lunxi, W. Liu and H. Wang, *J. Solid State Chem.*, 2021, **296**, 121956.

20 E. J. Maginn, R. A. Messerly, D. J. Carlson, D. R. Roe and R. Elliott, *J. Comput. Sci-Neth.*, 2018, **1**, 6324.

21 V. Sadiye and K. Seda, *J. Mater. Chem. A*, 2019, **7**, 2301–2314.

22 J. J. Wardzala, J. P. Ruffley, I. Goodenough, A. M. Schmidt and J. K. Johnson, *J. Phys. Chem. C*, 2020, **124**, 28469–28478.

23 B. Sütay and M. Yurtsever, *J. Mol. Model.*, 2017, **23**, 1–10.

24 W. D. Cornell, P. Cieplak, C. I. Bayly, I. R. Gould, K. M. Merz, D. M. Ferguson, D. C. Spellmeyer, T. Fox, J. W. Caldwell and P. A. Kollman, *J. Am. Chem. Soc.*, 1995, **117**, 5179–5197.

25 C. E. Wilmer, K. C. Kim and R. Q. Snurr, *J. Phys. Chem. Lett.*, 2012, **3**, 2506–2511.

26 B. Seger, *Z. Naturforsch A.*, 2005, **60**, 805–813.

27 A. K. Rappe, C. J. Casewit, K. S. Colwell, W. A. I. Goddard and W. M. J. Skiff, *J. Am. Chem. Soc.*, 1992, **114**, 10024–10035.

28 D. David, C. Sofia, E. D. Ellis and Q. S. Randall, *Mol. Simul.*, 2016, **42**, 81–101.

29 S. Plimpton, *J. Compute. Phys.*, 1995, **117**, 1–19.

30 S. Keskin and D. S. Sholl, *Langmuir*, 2009, **25**, 11786–11795.

31 D. Dubbeldam, D. C. Ford, D. E. Ellis and R. Q. Snurr, *Mol. Simul.*, 2009, **35**, 1084–1097.

32 X. Yu, S. Choi, D. Tang, A. J. Medford and D. S. Sholl, *J. Phys. Chem. C*, 2021, **125**, 18046–18057.

33 E. J. Maginn, R. A. Messerly, D. J. Carlson, D. R. Roe and R. Elliott, *J. Comput. Sci-Neth.*, 2018, **1**, 6324.

34 W. Hui, J. M. Simmons, G. Srinivas, Z. Wei and T. Yildirim, *J. Phys. Chem. Lett.*, 2010, **1**, 1946–1951.

35 A. Einstein, *Ann. Phys.*, 1911, **19**, 289.

36 E. W. Christopher, C. K. Ki and Q. S. Randall, *J. Phys. Chem. Lett.*, 2012, **17**, 2506–2511.

37 T. F. Willems, C. H. Rycroft, M. Kazi, J. C. Meza and M. Haranczyk, *Micropor. Mesopor. Mat.*, 2012, **149**, 134–141.

38 L. D. Gelb and K. E. Gubbins, *Langmuir*, 1999, **15**, 305–308.

39 K. S. Walton and R. Q. Snurr, *J. Am. Chem. Soc.*, 2007, **129**, 8552–8556.

40 J. G. Mcdaniel, S. Li, E. Tylianakis, R. Q. Snurr and J. R. Schmidt, *J. Phys. Chem. C*, 2015, **119**, 3143–3152.

41 Z. P. Athanassios, *Mol. Phys.*, 1987, **62**, 701–719.

42 D. I. Kolokolov, H. Jobic, A. G. Stepanov, J. Ollivier, S. Rives, G. Maurin, T. Devic, C. Serre and G. Férey, *J. Phys. Chem. C*, 2012, **116**, 15093–15098.

43 D. Peralta, K. Barthelet, J. Pérez-Pellitero, D. Peralta, K. Barthelet, J. Pérez-Pellitero, C. Chizallet, G. Chaplais, A. Simon-Masseron and G. D. Pirngruber, *J. Phys. Chem. C*, 2012, **116**, 21844–21855.

44 N. Divya, G. B. Deepti, B. Rahul and K. K. Ulhas, *J. Mater. Chem. A*, 2013, **1**, 8828–8835.

45 Z. Y. Gu, D. Q. Jiang, H. F. Wang, X. Y. Cui and X. P. Yan, *J. Phys. Chem. C*, 2010, **114**, 311–316.

46 L. Alaerts, C. E. Kirschhock, M. Maes, V. Finsy, A. Depla, J. A. Martens, G. V. Baron, P. A. Jacobs, J. F. Denayer and D. E. D. Vos, *Angew. Chem., Int. Ed.*, 2007, **46**, 4293.

47 M. A. Granato, V. D. Martins, A. F. P. Ferreira and A. E. Rodrigues, *Microporous Mesoporous Mater.*, 2014, **190**, 165–170.

48 L. Chen, D. D. Zhu, G. J. Ji, S. Yuan, J. F. Qian, M. Y. He, Q. Chen and Z. H. Zhang, *J. Chem. Technol. Biot.*, 2018, **93**, 2898–2905.

49 M. I. Gonzalez, M. T. Kapelewski, E. D. Bloch, P. J. Milner, D. A. Reed, M. R. Hudson, J. A. Mason, G. Barin, C. M. Brown and J. R. Long, *J. Am. Chem. Soc.*, 2018, **140**, 3412–3422.

50 J. A. Gee, K. Zhang, S. Bhattacharyya, J. Bentley, M. Rungta, J. S. Abichandani, D. S. Sholl and S. Nair, *J. Phys. Chem. C*, 2016, **120**, 12075.

51 J. M. Castillo, T. J. H. Vlugt and S. Calero, *J. Phys. Chem. C*, 2009, **113**, 20869–20874.

52 V. Finsy, H. Verelst, L. Alaerts, D. E. D. Vos, P. A. Jacobs, G. V. Baron and E. M. J. Denayer, *J. Am. Chem. Soc.*, 2008, **130**, 7110.

53 L. Alaerts, M. Maes, L. Giebeler, P. A. Jacobs, J. A. Martens, J. F. Denayer, C. E. Kirschhock and D. E. D. Vos, *J. Am. Chem. Soc.*, 2008, **130**, 14170.

54 M. Maes, F. Vermoortele, L. Alaerts, S. Couck, C. E. A. Kirschhock, J. F. M. Denayer and D. E. DeVos, *J. Am. Chem. Soc.*, 2010, **132**, 15277–15285.

55 B. M. Krooss, F. V. Bergen, Y. Gensterblum, N. Siemons, H. J. M. Pagnier and P. David, *Int. J. Coal Geol.*, 2002, **51**, 69–92.

56 V. Finsy, H. Verelst, L. Alaerts, D. E. D. Vos, P. A. Jacobs, G. V. Baron and J. E. M. Denayer, *J. Am. Chem. Soc.*, 2008, **130**, 7110.

57 Z. T. Yan, Y. J. Gong, B. H. Chen, X. N. Wu, Q. liu, L. l. Cui, S. S. Xiong and S. M. Peng, *J. Phys. Chem. C*, 2019, **239**, 116514.

58 C. R. Clarkson and R. M. Bustin, *Int. J. Coal Geol.*, 2000, **42**, 241–271.

59 J. P. Nan, X. L. Dong, W. J. Wang, W. Q. Jin and N. P. Xu, *Langmuir*, 2011, **27**, 4309–4312.